An averaged mass correction scheme for the simulation of high subsonic turbulent internal flows using a lattice Boltzmann method

Jingtao Ma, Lincheng Xu, Jérôme Jacob, Eric Serre, Pierre Sagaut

▶ **To cite this version:**

Jingtao Ma, Lincheng Xu, Jérôme Jacob, Eric Serre, Pierre Sagaut. An averaged mass correction scheme for the simulation of high subsonic turbulent internal flows using a lattice Boltzmann method. Physics of Fluids, 2024, 36 (3), 10.1063/5.0192360 . hal-04514161

HAL Id: hal-04514161
https://hal.science/hal-04514161

Submitted on 21 Mar 2024

HAL is a multi-disciplinary open access archive for the deposit and dissemination of scientific research documents, whether they are published or not. The documents may come from teaching and research institutions in France or abroad, or from public or private research centers.

L'archive ouverte pluridisciplinaire **HAL**, est destinée au dépôt et à la diffusion de documents scientifiques de niveau recherche, publiés ou non, émanant des établissements d'enseignement et de recherche français ou étrangers, des laboratoires publics ou privés.

High subsonic turbulent internal flow simulations using the lattice Boltzmann method with mass correction

Jingtao Ma,[1] Jérôme Jacob,[1] Lincheng Xu,[2, a)] Eric Serre,[1] and Pierre Sagaut[1]

[1)]*Aix Marseille Univ, CNRS, Centrale Marseille, M2P2, Marseille, France*

[2)]*School of Aeronautics, Northwestern Polytechnical University, Xi'an, China*

(Dated: 23 June 2023)

In this study, we have presented a numerical investigation of high subsonic compressible turbulent flows using the pressure-based lattice Boltzmann method coupled with the Spalart-Allmaras turbulent model. The major objective of the present study is to evaluate the mass leakage issue in compressible turbulent flows and assess the effectiveness of a previously proposed averaged mass correction technique originally designed for incompressible flows. The compressible turbulent flows in inclined straight channels and a NASA Glenn S-duct are examined for this purpose. The findings indicate that mass leakage can be a significant concern in compressible turbulent channel flows across all Mach numbers considered in this study ($Ma = 0.2, 0.5$, and 0.8). In the aligned channel cases, symmetric distributions of cross-sectional velocity and skin frictions at the top and bottom walls are observed, even when the mass leakage correction is absent. However, a linear decrease in the mass flux along the channel is observed without mass correction. In inclined cases, the presence of mass leakage disrupts the symmetric distributions of cross-sectional velocity and skin frictions. Significant improvements in the symmetry of skin friction and sectional velocity profiles are observed when the mass correction is employed. In addition, the capability of the compressible solver to study complex three-dimensional flows was evaluated by investigating compressible turbulent flow in a NASA Glenn S-duct. The obtained results demonstrate good agreement with previous experimental and numerical data on the static pressure coefficient along three streamwise lines on the surface of the S-duct. This proves the capability of the present method to capture complex three-dimensional phenomena in compressible flows.

[a)]lincheng.xu@nwpu.edu.cn

I. INTRODUCTION

The lattice Boltzmann method (LBM) has emerged as a prevailing simulation method in computational fluid dynamics, offering numerous advantages over classic numerical methods based on the Navier-Stokes equations. LBM is rooted in particle kinetics, and it is characterized by the localized nature in the streaming-collision processes, as well as the inherent simplicity of the LB equations. These features make LBM a powerful tool for analyzing various flow problems, including but not limited to porous media[1–3], fluid-structure interaction[4,5], turbulent flow[6–8], and etc.

Compared with other numerical methods relying on macroscopic quantities, the treatment of boundary conditions in LB frame holds particularly significant importance[9]. This is particularly true when LBM is coupled with the immersed boundary method (IBM) for non-body-fitted meshes. At a boundary, the presence of distribution functions streaming from non-fluid regions is normally inevitable, and it means the some missing distribution functions at the boundary grid need be determined before the collision step. To determine the missing distribution functions, the simplest method is to use the bounce-back scheme[10], in which distribution functions streaming from the grid nodes are directly returned along the reversed directions. However, the accuracy of the boundary-back scheme is merely first order[11], which may ruin the overall second-order accuracy of LBM. Therefore, some improvements on the boundary-back scheme were proposed, for example, reconstruction distribution functions with interpolation or extrapolation method[12,13]. Except for the bounce-back scheme, there are also some other second-order accurate boundary treatments proposed, which are normally based on construction of distribution functions at boundary nodes (e.g., the non-equilibrium extrapolation scheme[14]). However, the mass conservation is normally compromised during the process of the interpolation (or extrapolation) and reconstruction, which can cause mass leakage.

To eliminate the mass leakage involved in the boundary treatment in LBM, great efforts have been made[15–18]. For example, a local second-order accurate boundary treatment scheme was proposed by Ginzburg and d'Humières to give exact results without mass error in Couette and Poiseuille flows[15]. Bao *et al.* enforced the mass conservation by directly modifying local density values when studying the flow in a U-shape tube[16]. However, the origin of the mass leakage in LBM have not been analyzed systematically until the recent paper by Xu *et al.*[19], where the source of the mass leakage was theoretically derived (e.g., the gradients of density, normal momentum,

and normal momentum flux at the solid boundary), and two different mass correction schemes were utilized to get rid of the mass leakage on boundary nodes. It has been found that the mass leakage can be a big issue in flows at high Reynolds numbers (e.g., turbulent flows), and it can ruin the symmetric distributions of the cross-sectional velocity[19]. However, this study have only focused on incompressible flows, where the gradients of density and momentum are negligible for a stationary boundary. In a compressible flow, the gradients of density and momentum at boundaries nodes may no longer be negligible. Therefore, it is beneficial to examine the mass leakage in compressible turbulent flows and to evaluate the effectiveness of the mass correction schemes propose in Ref.[19].

Recently, a pressure-based lattice Boltzmann method have been developed to investigate compressible flows[20], and it has been proved to be an powerful technique for high subsonic and supersonic compressible flow[20–22]. In addition, the mass leakage in flows dominated by large temperature difference was investigated in Wang *et al.*[23], and the local mass correction scheme was confirmed to be effective to mitigate mass leakage in low-Ma compressible flows. However, this investigation did not address the issue of mass leakage in high-speed flows, where the local mass correction scheme becomes ineffective[19]. Here, the pressure-based LBM is combined with the RANS turbulent model (Spalart-Allmaras) to examine the capability of the pressure-based solver for turbulent compressible flows, and the mass leakage issue in the high subsonic compressible turbulent flows are studied. The organisation of the rest of this paper is as follows. The governing equations of the fluid dynamics and the mathematical models utilized in the present work is introduced in Section II. In Section III, the numerical methods used are presented. Section IV gives the results and discussion. Final conclusions are provided in Section V.

II. MATHEMATICAL MODELS

A. Governing equations for fluid dynamics

The dynamics of a steady-state mean compressible flow are governed by the following RANS equations,

$$\frac{\partial \bar{\rho}}{\partial t} + \nabla \cdot (\bar{\rho}\hat{\boldsymbol{u}}) = 0, \tag{1}$$

$$\frac{\partial \bar{\rho}\hat{\boldsymbol{u}}}{\partial t} + \nabla \cdot (\bar{\rho}\hat{\boldsymbol{u}}\hat{\boldsymbol{u}}) = -\nabla \bar{p} + \nabla \cdot \hat{\boldsymbol{\tau}}, \tag{2}$$

$$\frac{\partial \bar{\rho}\hat{E}}{\partial t} + \nabla \cdot (\bar{\rho}\hat{H}\hat{\boldsymbol{u}}) = \nabla \cdot (\lambda \nabla \hat{T}) + \nabla \cdot (\hat{\boldsymbol{u}} \cdot \boldsymbol{\tau}), \tag{3}$$

where $\bar{()}$ represents the conventional time-average mean, and $\hat{()}$ Favre (density-weighted) average. $\bar{\rho}$ is the density, $\hat{\boldsymbol{u}}$ is the velocity vector, t is time, $\bar{p}$ is the pressure, $\hat{\boldsymbol{\tau}}$ is the total shear stress tensor, λ is the heat conductivity, $\hat{E} = \hat{e} + \|\hat{\boldsymbol{u}}\|^2/2$ is the total energy, and $\hat{H} = \hat{E} + \bar{p}/\bar{\rho}$ is the total enthalpy. The internal energy $\hat{e}$ is defined by $\hat{e} = C_v \hat{T}$, with C_v being the mass specific heat capacity at constant volume. The total stress tensor $\hat{\boldsymbol{\tau}}$ consists of the viscous stress part and the Reynolds stress part

$$\hat{\boldsymbol{\tau}} = \hat{\boldsymbol{\tau}}^{\nu} + \hat{\boldsymbol{\tau}}^{R} \tag{4}$$

where the viscous stress tensor is determined as

$$\hat{\boldsymbol{\tau}}^{\nu} = \mu \left[\nabla \hat{\boldsymbol{u}} + (\nabla \hat{\boldsymbol{u}})^T - \frac{2}{3}(\nabla \cdot \hat{\boldsymbol{u}})\boldsymbol{I} \right], \tag{5}$$

with μ being the dynamic and eddy viscosity, and following the Boussinesq approximation, the Reynolds stress is given as

$$\hat{\boldsymbol{\tau}}^{R} = \mu_t \left[\nabla \hat{\boldsymbol{u}} + (\nabla \hat{\boldsymbol{u}})^T - \frac{2}{3}(\nabla \cdot \hat{\boldsymbol{u}})\boldsymbol{I} \right], \tag{6}$$

where μ_t is the eddy viscosity determined via a turbulent model. To close the above system, the equation of state for the perfect gas is considered,

$$\bar{p} = \bar{\rho} r \hat{T} \tag{7}$$

where $r = R/W$ being the specific gas constant, with R and W respectively being the universal gas constant and the molecular weight. According to dry air properties, $r = 2.9 \times 10^5$ J kg^{-1} K^{-1} will be utilized in this work.

It should be noted that the energy conservation can also be expressed in terms of entropy $\hat{s}$ as [24,25]

$$\frac{\partial \hat{s}}{\partial t} + \hat{\boldsymbol{u}} \cdot \nabla \hat{s} = \frac{1}{\bar{\rho}\hat{T}} \nabla \cdot (\lambda \nabla \hat{T}) + \frac{1}{\bar{\rho}\hat{T}} \hat{\boldsymbol{\tau}} : \nabla \hat{\boldsymbol{u}}. \tag{8}$$

where the entropy $\hat{s}$ can be expressed as

$$\hat{s} = C_v \ln \frac{\bar{p}}{\bar{\rho}^{\gamma}}, \tag{9}$$

when the calorically perfect gas (constant specific heat C_p and C_v, for constant pressure and volume process, respectively) is assumed, and $\gamma = C_p/C_v$ is the adiabatic exponent. The practical use of entropy $\hat{s}$ instead of $\hat{E}$ to enforce the energy conservation has been widely validated[20,23,24], and the entropy $\hat{s}$ on boundary nodes are normally determined using the temperature $\hat{T}$.

Here, the eddy viscosity μ_t is determined using the Spalart-Allmaras (SA) turbulence model, and the SA model with a f_{v3} is utilized in this study[6,7]. Detailed description on the SA model can be found in Appendix A.

III. NUMERICAL METHOD

A. The pressure-based lattice Boltzmann method for mass and momentum conservation

Here, a brief introduction about the pressure-based lattice Boltzmann method is given, and readers are recommended to refer to Refs.[20,21,23] to more details about this method.

The discrete equation with a single relaxation time for the pressure-based lattice Boltzmann method is given as [20,23],

$$f_i\left(\boldsymbol{x}+\boldsymbol{e}_i\Delta t, t+\Delta t\right) - f_i(\boldsymbol{x},t) = -\frac{1}{\tau}\left[f_i(\boldsymbol{x},t) - f_i^{eq}(\boldsymbol{x},t)\right] + \frac{\Delta t}{2}F_i, \tag{10}$$

where f_i is the particle distribution function, t is time, $\boldsymbol{x}$ is the fluid parcel position, $\boldsymbol{e}_i$ is the discrete velocity along the ith direction, Δt is the time step, f_i^{eq} is the equilibrium distribution function, τ is the non-dimensional relaxation time, and F_i represents the force term exerted on the distribution function.

The equilibrium distribution function is computed as [23]

$$\begin{aligned} f_i^{eq} = w_i \Bigg[& \rho\theta + \frac{\boldsymbol{e}_{i\alpha}}{c_s^2}\rho u_\alpha + \frac{\boldsymbol{e}_{i\alpha}\boldsymbol{e}_{i\beta} - c_s^2\delta_{\alpha\beta}}{2c_s^4} : \rho u_\alpha u_\beta \\ & + \frac{\boldsymbol{e}_{i\alpha}\boldsymbol{e}_{i\beta}\boldsymbol{e}_{i\gamma} - c_s^2\left[\boldsymbol{e}_i\delta\right]_{\alpha\beta\gamma}}{6c_s^6} : \rho u_\alpha u_\beta u_\gamma \Bigg] \end{aligned} \tag{11}$$

where w_i is the weight factor associated with the discrete velocity $\boldsymbol{e}_i$, $\theta = T/T_{\text{ref}}$ is the normalized temperature with T_{ref} being the reference temperature, u_α is the αth velocity component with α, β, and γ being coordinate indices, and $\left[\boldsymbol{e}_i\delta\right]_{\alpha\beta\gamma} = \boldsymbol{e}_{i\alpha}\delta_{\beta\gamma} + \boldsymbol{e}_{i\beta}\delta_{\alpha\gamma} + \boldsymbol{e}_{i\gamma}\delta_{\alpha\beta}$. Please note that the Einstein summation convention is applied in Eq. 11.

In the pressure-based LB frame, the first three moments of the distribution function are expressed as [20,23]

$$\begin{aligned} \sum f_i = p/c_s^2 = \rho\theta, \quad \sum f_i \boldsymbol{e}_i = \rho \boldsymbol{u}, \\ \sum f_i \boldsymbol{e}_i \boldsymbol{e}_i = \rho \boldsymbol{u}\boldsymbol{u} + p\mathbf{I}, \end{aligned} \tag{12}$$

where c_s is the speed of sound and $\mathbf{I}$ is the identity matrix.

By solving Eq. 10, the compressible momentum equation (Eq. 2) can be fully restored, but the mass conservation is not directly enforced. Alternatively, the mass conservation is achieved by solving Eq. 1 with the traditional finite-difference method as [20,23]

$$\begin{aligned} \frac{\rho(t+\Delta t, \boldsymbol{x}) - \rho(t, \boldsymbol{x})}{\Delta t} &= -\nabla(\rho \boldsymbol{u}) + O(\Delta t) \\ &= \sum \frac{f_i(t+\Delta t, \boldsymbol{x}) - f_i^{col}(t, \boldsymbol{x})}{\Delta t}. \end{aligned} \tag{13}$$

where f_i^{col} is the post-collision distribution function. Then, the fluid density is updated as [20,23]

$$\begin{aligned} \rho(t+\Delta t, \boldsymbol{x}) &\approx -\frac{\partial \rho u_\alpha}{\partial x_\alpha} \Delta t + \rho(t, \boldsymbol{x}) \\ &= (\rho\theta)(t+\Delta t, \boldsymbol{x}) - (\rho\theta)(t, \boldsymbol{x}) + \rho(t, \boldsymbol{x}) \\ &= \sum_i f_i(t+\Delta t, \boldsymbol{x}) - \rho(t, \boldsymbol{x})\theta(t, \boldsymbol{x}) + \rho(t, \boldsymbol{x}). \end{aligned} \tag{14}$$

It should be note that the hybrid recursive regularized collision model (HRR-BGK) is normally utilized to improve the numerical stability in turbulent flows, and detailed description of HRR-BGK can be found in Refs.[24,26].

B. The finite difference method for the entropy equation and transportation equation for the Spalart-Allmaras model

To couple the energy conservation with the LBM solver, an entropy equation under non-conservative format is solved using the second-order finite difference method[21,23],

$$\underbrace{\frac{\partial s}{\partial t} + u_\beta \frac{\partial s}{\partial x_\beta}}_{\text{MUSCL-Hancock}} = \underbrace{\frac{1}{\rho T}\left[\Pi_{\alpha\beta}\frac{\partial u_\alpha}{\partial x_\beta} - \frac{\partial q_\beta}{\partial x_\beta}\right]}_{\text{Finite difference - second order}}. \tag{15}$$

The MUSCL-Hancock method is employed to discretize the temporal derivative and the convective flux in Eq. 15. This particular scheme is characterized as non-local and necessitates a

five-point stencil in each direction. However, when dealing with boundary conditions in close proximity, this stencil may not always be available. In such cases, a combination of a second-order centered flux (to properly incorporate the boundary condition) and upwinding (for numerical stability) is utilized. The calculation of thermal conduction and viscous heat employs a simple second-order centered finite difference scheme, which incorporates a first-order decentered procedure for nodes near the boundaries. For more information about the method, please refer to references by Wang *et al.*[23] and Coratger *et al.*[21].

In actual simulations, the transportation equation of the Spalart-Allmaras model (Equation A3) is commonly reformulated using the non-dimensional variable $\chi = \tilde{v}/v$. To solve the equations of the SA model, a second-order accurate finite difference scheme is employed [6,7]. The temporal derivative term is discretized using a first-order forward Euler scheme. For the advection term, a hybrid upwind-centered scheme is utilized. Gradients and Laplacian operators are calculated using a centered scheme. In the regularized BGK model, the eddy viscosity v_t obtained from the SA model is incorporated into the relaxation time as $\tau = \frac{1}{2} + \frac{v+v_t}{c_s^2}$, allowing for the consideration of turbulence effects in the collision operator [6].

C. Wall model

For the simulations of turbulent flows at high Reynolds numbers, a great challenge is the requirement of large numbers of grid nodes in the near-wall region to capture the rapid change of the flow quantities. To tackle this problem, a practical way is to adopt the modelled approach, which has been widely employed by previous numerical investigations. In this section, the wall model utilized in this work is introduced.

Here, we introduce the following non-dimensionalization,

$$u^+ = \frac{u}{u_\tau}, \quad y^+ = \frac{u_\tau d}{\nu}, \tag{16}$$

where u_τ and ν are respectively the friction velocity and the fluid kinematic viscosity, and the classic logarithm wall law can be expressed as [6,7]

$$u^+ = \begin{cases} y^+, & \text{in the viscous sublayer,} \\ \frac{1}{\kappa}\log(y^+) + B, & \text{in the inertial layer,} \end{cases} \tag{17}$$

where $\kappa \approx 0.41$ and $B \approx 5.0$. However, the logarithm law normally involves an iterative process to calculate the friction velocity, and this process can slow down the whole simulation. Therefore, an explicit power-law based wall model was used in Wilhelm *et al.*[6] to avoid the iterative process. In this model, the logarithmic behaviour of the velocity profile in the inertial layer is approximated by the power law, and the linear law is retained for the viscous sublayer. This model can be expressed as follows [7],

$$u^+ = \begin{cases} f_{\text{lam}}\left(y^+\right) = y^+, & \text{if } y^+ \le y^+_{\text{lam}} \text{ or } Re_y \le Re_c \\ f_{\text{pow}}\ \left(y^+\right) = A\left(y^+\right)^B, & \text{if } y^+ > y^+_{\text{lam}} \text{ or } Re_y > Re_c \end{cases} \tag{18}$$

where $B = 1/7$, and A is determined by the the continuity of the velocity profile at $y^+_{\text{lam}} = 11.81$ as $A = \left(y^+_{\text{lam}}\right)^{1-B} \approx 8.3$. Please note that in the simulation, which profile to use is determined based on the availability of u_τ. If u_τ is available, then y^+ is used and compared with y^+_{lam}. Otherwise, the local Reynolds number $Re_y = yu/\nu = y^+u^+$ is used and compared with the critical Reynolds number $Re_c = \left(y^+_{\text{lam}}\right)^2$.

The explicit power-law based wall model mentioned above relies on the equilibrium assumption for the turbulent boundary layer under zero pressure gradient. Therefore, it is anticipated that this model may not provide accurate results for flows experiencing substantial adverse pressure gradients. To simulate a flow with strong adverse pressure gradients, the adverse pressure gradient log-law model proposed in Ref.[27] is employed in the present study. Please refer to Ref.[27] for detailed description on this model.

D. Mass leakage quantification and mass correction schemes

The local mass leakage in LBM defined as the net loss of distribution functions during the streaming process at a boundary node takes the form as [19]

$$E(\boldsymbol{x}) = \frac{\Delta x}{\Delta t} \sum_{\boldsymbol{x}+\boldsymbol{e}_i\Delta t \in \Gamma} \left[f_i^{col}(\boldsymbol{x}) - f_{\bar{i}}^{col}\left(\boldsymbol{x}+\boldsymbol{e}_i\Delta t\right) \right], \tag{19}$$

where $\boldsymbol{x}$ is the coordinate vector of a boundary node, Γ represents the non-fluid region, Δx is the grid spacing, Δt is the time step, $\boldsymbol{e}_i$ is the ith discrete velocity with its components taking values among 0 and $\pm\Delta x/\Delta t$, and $\bar{i}$ is the opposite direction of the ith direction (i.e., $\boldsymbol{e}_i = -\boldsymbol{e}_{\bar{i}}$). Clearly, it can be found that the mass leakage E actually represents the local mass flux across the boundary [19], i.e.,

$$
\begin{aligned}
E(\boldsymbol{x}) &= \frac{\Delta x}{\Delta t} \sum_{\boldsymbol{x}+\boldsymbol{e}_i\Delta t\in\Gamma} \left[f_i^{col}(\boldsymbol{x}) - f_{\bar{i}}^{col}(\boldsymbol{x}+\boldsymbol{e}_i\Delta t) \right] \\
&\approx \sum f_{i,w}\,\mathrm{Sign}\left(\boldsymbol{e}_i\cdot\boldsymbol{n}\right) \approx \sum f_{i,w}\boldsymbol{e}_i\cdot\boldsymbol{n} = \rho\boldsymbol{u}_w\cdot\boldsymbol{n},
\end{aligned}
\tag{20}
$$

where w represents the solid boundary involved, $\boldsymbol{u}_w$ is the local velocity of fluid across the solid boundary w, and $\boldsymbol{n}$ is the local outward normal vector at the boundary.

Based on the definition of the local mass leakage, it is straightforward to apply the local mass correction scheme (LMC) by compensate the local mass loss as[19]

$$
\Delta\rho(\boldsymbol{x}) = \frac{\Delta t}{\Delta x}E(\boldsymbol{x}) = \sum_{\boldsymbol{x}+\boldsymbol{e}_i\Delta t\in\Gamma} \left[f_i(\boldsymbol{x}) - f_{\bar{i}}(\boldsymbol{x}+\boldsymbol{e}_i\Delta t) \right]. \tag{21}
$$

The local mass correction scheme aligns with the widely employed bounce-back (BB) method, but it has been demonstrated this scheme can include a zeroth-order perturbation to the solution of density (Please refer to Xu *et al.*[19] for detailed analysis). Therefore, the averaged mass correction scheme (AMC) was proposed, and it is formulated as

$$
\begin{aligned}
\Delta\rho(\boldsymbol{x}) &= \frac{\Delta t}{\Delta x}\bar{E}(\boldsymbol{x}) = \frac{\Delta t}{\Delta x}\frac{\sum_\Omega E\Delta S}{\sum_\Omega \Delta S} \\
&= \frac{\sum_\Omega \left\{ \sum_{\boldsymbol{x}+\boldsymbol{e}_i\Delta t\in\Gamma} \left[f_i(\boldsymbol{x}) - f_i\left(\boldsymbol{x}+\boldsymbol{e}_i\Delta t\right) \right] \right\} \Delta S}{\sum_\Omega \Delta S}
\end{aligned}
\tag{22}
$$

where Ω represents the solid boundary and $\bar{E} = \sum_\Omega E\Delta S / \sum_\Omega \Delta S$ is the averaged mass leakage over the boundary. It has bee reported that the averaged mass correction scheme can effectively mitigate the mass leakage in incompressible turbulent flows. Therefore, this scheme is utilized to enforce mass conservation in this study. However, as stated in Wang *et al.*[23], the mass correction schemes (Eqs. 21 and 22) can not be directly applied in the pressure-based lattice Boltzmann frame, due to the complex relationship between the distribution function f_i and the density ρ. Therefore, the local mass leakage is expressed in the form of macroscopic quantities as,

$$
E(\boldsymbol{x}) = \frac{\Delta x}{\Delta t}\left[\rho^{BB}(\boldsymbol{x}) - \rho(\boldsymbol{x}) \right], \tag{23}
$$

where $\rho^{BB} = \sum\limits_{\boldsymbol{x}+\boldsymbol{e}_i\Delta t\in\Omega} f_i^{col}(\boldsymbol{x}) + \sum\limits_{\boldsymbol{x}+\boldsymbol{e}_i\Delta t\in F} f_{\bar{i}}^{col}(\boldsymbol{x}+\boldsymbol{e}_i\Delta t)$ is the density obtained using the BB strategy at a boundary node, with F representing the fluid region. Within the frame of pressure-based LB, the ρ^{BB} can be calculated as[23]

$$\begin{aligned}
&\rho^{BB}(t+\Delta t,\boldsymbol{x}) \\
&\quad=\rho(t,\boldsymbol{x})+\left[\sum_{x+\boldsymbol{e}_i\Delta t\in\Omega} f_i^{col}(t,\boldsymbol{x})+\sum_{\boldsymbol{x}+\boldsymbol{e}_i\Delta t\in F} f_{\bar{i}}^{col}(t,\boldsymbol{x}+\boldsymbol{e}_i\Delta t)\right] \\
&\qquad-\rho(t,\boldsymbol{x})\theta(t,\boldsymbol{x}).
\end{aligned} \tag{24}$$

In this case, the local density correction can be applied as

$$\begin{aligned}
\Delta\rho(t+\Delta t,\boldsymbol{x}) &=\frac{\Delta t}{\Delta x}E(t+\Delta t,\boldsymbol{x}) \\
&=\rho(t,\boldsymbol{x})+\sum_{x+e_i\Delta t\in\Omega} f_i^{col}(t,\boldsymbol{x})+\sum_{x+e_i\Delta t\in F} f_{\bar{i}}^{col}(t,\boldsymbol{x}+\boldsymbol{e}_i\Delta t) \\
&\quad-\rho(t,\boldsymbol{x})\theta(t,\boldsymbol{x})-\rho(t+\Delta t,\boldsymbol{x}).
\end{aligned} \tag{25}$$

The effectiveness of the local mass correction scheme (Eq. 25) in mitigating mass leakage in low-*Ma* compressible flows has been confirmed[23]. However, the formulation of the averaged mass correction scheme for high-Reynolds-number compressible turbulent flows is still pending. In this study, we apply the averaged density correction for high subsonic compressible flows in the pressure-based LB framework by averaging the total mass leakage over the entire solid boundary as

$$\begin{aligned}
\Delta\rho(t+\Delta t,\boldsymbol{x}) &=\frac{\Delta t}{\Delta x}\bar{E}(t+\Delta t,\boldsymbol{x})=\frac{\Delta t}{\Delta x}\frac{\sum_\Omega E\Delta S}{\sum_\Omega \Delta S} \\
&=\sum_\Omega\Bigg[\rho(t,\boldsymbol{x})+\sum_{x+e_i\Delta t\in F}=f_{\bar{i}}^{col}(t,\boldsymbol{x})\,(t,\boldsymbol{x}+\boldsymbol{e}_i\Delta t) \\
&\quad+\sum_{x+e_i\Delta t\in\Omega} f_i^{col}(t,\boldsymbol{x})-\rho(t,\boldsymbol{x})\theta(t,\boldsymbol{x})-\rho(t+\Delta t,\boldsymbol{x})\Bigg]\Delta S/\sum_\Omega\Delta S.
\end{aligned} \tag{26}$$

IV. RESULTS AND DISCUSSION

A. The compressible turbulent flow in a straight channel with variously inclined boundaries

In this section, the two-dimensional compressible turbulent flow in a straight channel with zero pressure gradient is investigated. The schematic diagram for the this problem and configurations of boundary conditions are shown in Figure 1. The straight channel is inclined with respect of the horizontal line at different inclination angles θ. To achieve the fully developed turbulent flow,

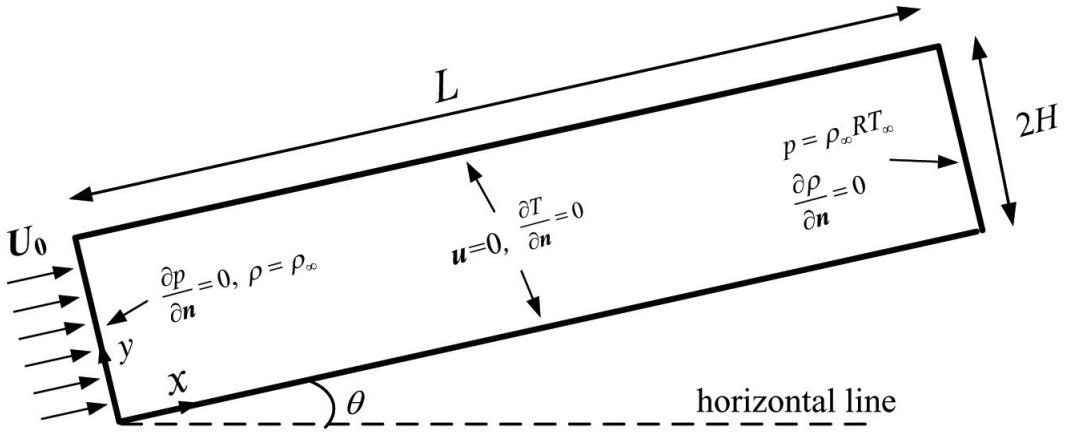

FIG. 1. The schematic diagram for the compressible turbulent flow in an inclined channel.

a long channel with the length of $L = 200H$ (with H being the half height of the channel) is utilized. The identical geometry has been used in the investigation on the incompressible turbulent channel flow[19]. The uniform flow with the velocity of U_0 is applied to the inlet of the channel, and a constant pressure is imposed at the outlet. The top and bottom boundaries of the channel are considered to be non-slip adiabatic walls. A small segment of a free-slip wall is inserted ahead of the channel to mitigate the impact of the inlet boundary condition, and a sponge layer is applied at the inlet to minimize the spurious reflections. To investigate the impact of the inclination angle θ on the issue of mass leakage, we analyze the problem using three distinct inclination angles ($\theta = 0^\circ, 15^\circ$ and 30°). The Reynolds number based on the half-height of the channel $Re = \rho_\infty U_0 H/\mu_0$ ranges from 4.8×10^4 to 1.92×10^5 depending on the inlet velocity, and the Mach numbers used are $Ma = U_0/\sqrt{\gamma RT_\infty} = 0.2$, 0.5 and 0.8. The acoustic Courant-Friedrichs-Lewy (CFL) number with respect to infinite state is defined as $\mathrm{CFL} = \frac{|U_0|+\sqrt{\gamma RT_\infty}}{\Delta x/\Delta t}$, and $\mathrm{CFL} = 0.5$ is utilized in this section. The uniform grid $\Delta x/H = 0.05$ is used in all simulations. Here, we focus on the effects of the Mach number and inclination angle on the issue of mass leakage in this problem.

1. *Effects of Ma*

The effects of the Mach number on the issue of mass leakage in the compressible turbulent channel flow are examined in this section. Here, only the aligned cases ($\theta = 0^\circ$) are considered, and discussion on the impact of the inclination angle on the mass leakage issue can be found in Section IV A 2.

First, the mass leakage issue at a low Mach number ($Ma = 0.2$) is evaluated. Figure 2(a) and (b) show the comparison of profiles of the sectional velocity and the skin friction along the channel at $Ma = 0.2$ for cases with and without the implementation of the mass correction scheme. The present results are compared with the previous benchmark DNS data[28] as the validation of the present method. It is found that the present results shown good agreemtn with the DNS data, which conforms the accuracy of the present method in compressible flow at low Ma. In addition, it is also observed that the sectional velocity show symmetric distributions about the centerline of the channel ($y/H = 1.0$), regardless of the utilization of the mass correction scheme. In addition, the skin frictions at top and bottom walls are identical. This is understandable since the mesh is symmetric for the aligned cases. Furthermore, the sectional velocity with the mass correction is slightly larger than that without mass correction. This is due to the elimination of mass leakage and the addition of mass flux through the mass correction. However, there exists small mass leakage in the case without mass correction (NMC). As shown in Figure 2(c), the sectional mass flux decreases linearly along the channel without the mass correction, and the variants can be over 1.2%. This is caused by the gradient of the density and momentum at the top and bottom boundaries. With the mass correction, the variants of the mass flux is reduced significantly to within 0.2%, which proves the effectiveness of the mass correction scheme on the compressible turbulent flow at low Mach numbers.

To evaluate the mass leakage issue in high subsonic compressible turbulent channel flows, simulations are also conducted at $Ma = 0.5$ and 0.8. Figure 3 shows the results at $Ma = 0.5$ and 0.8. It is observed that the sectional velocities and skin frictions at $Ma = 0.5$ and 0.8 also show symmetric distributions as in $Ma = 0.2$, and there is small differences between the results with and without mass correction. However, the variants of the mass flux is much larger in the results without mass correction (over 3.8%) at $Ma = 0.5$, which means the mass leakage can be more serious at higher speed flows. In addition, the variants of the mass flux is remarkably reduced to within 0.2%, when the averaged mass correction scheme is utilized. Similar tendencey has also

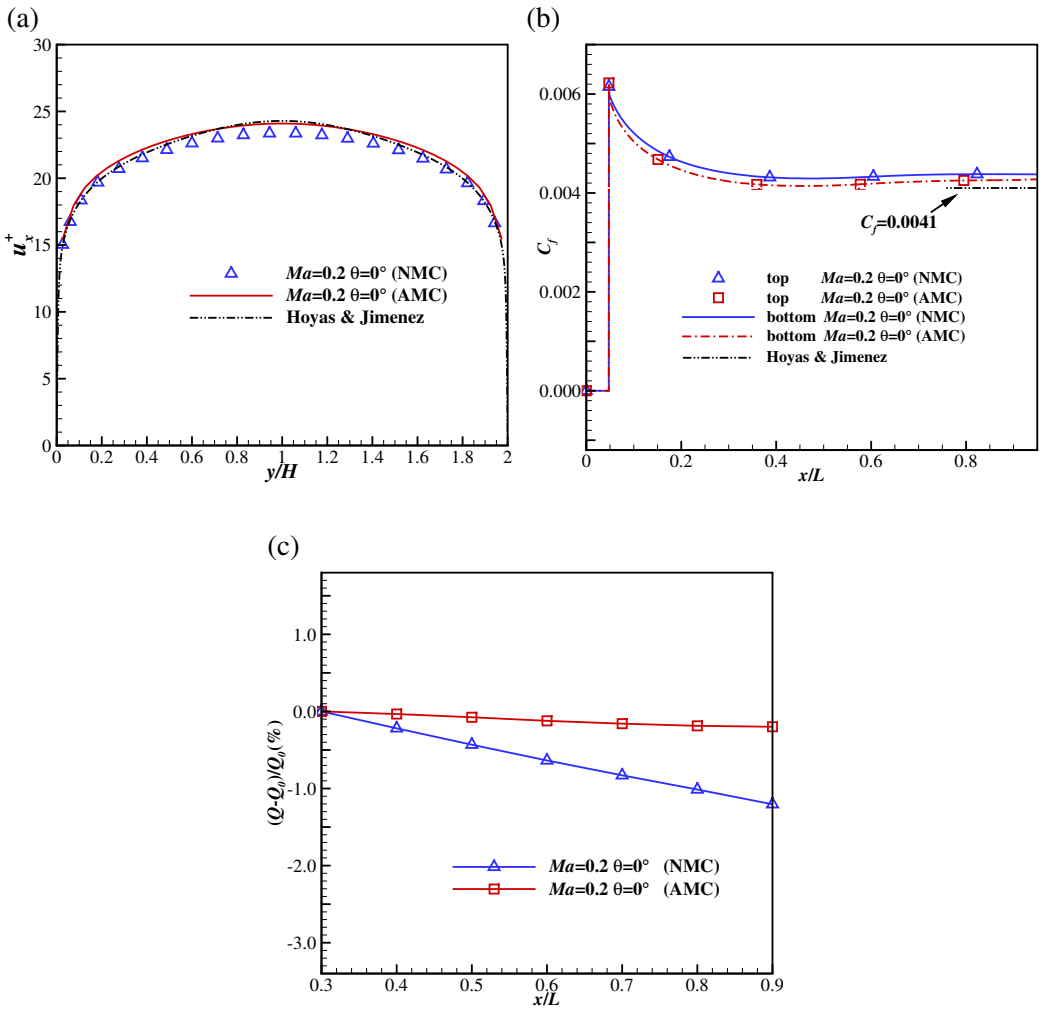

FIG. 2. The profiles of (a) the sectional velocity and (b) the skin friction at $Ma = 0.2$ and $\theta = 0°$. (c) The sectional mass flux variation along the channel. "NMC" and "AMC" respectively represent results without and with mass correction.

been observed at $Ma = 0.8$ (as shown in Figure 3).

2. *Effects of* θ

This section evaluates the effects of the inclination angle θ on the mass leakage issue in compressible turbulent channel flow. Figure 4(a) illustrates the profiles of the sectional velocity at $Ma = 0.2$ for $\theta = 15°$ and $30°$. It is observed that the sectional velocities at $\theta = 15°$ and $30°$ deviate from the symmetric profiles observed in the aligned case ($\theta = 0°$), which is consistent with the previous findings in incompressible turbulent flow within an inclined channel[19]. This deviation

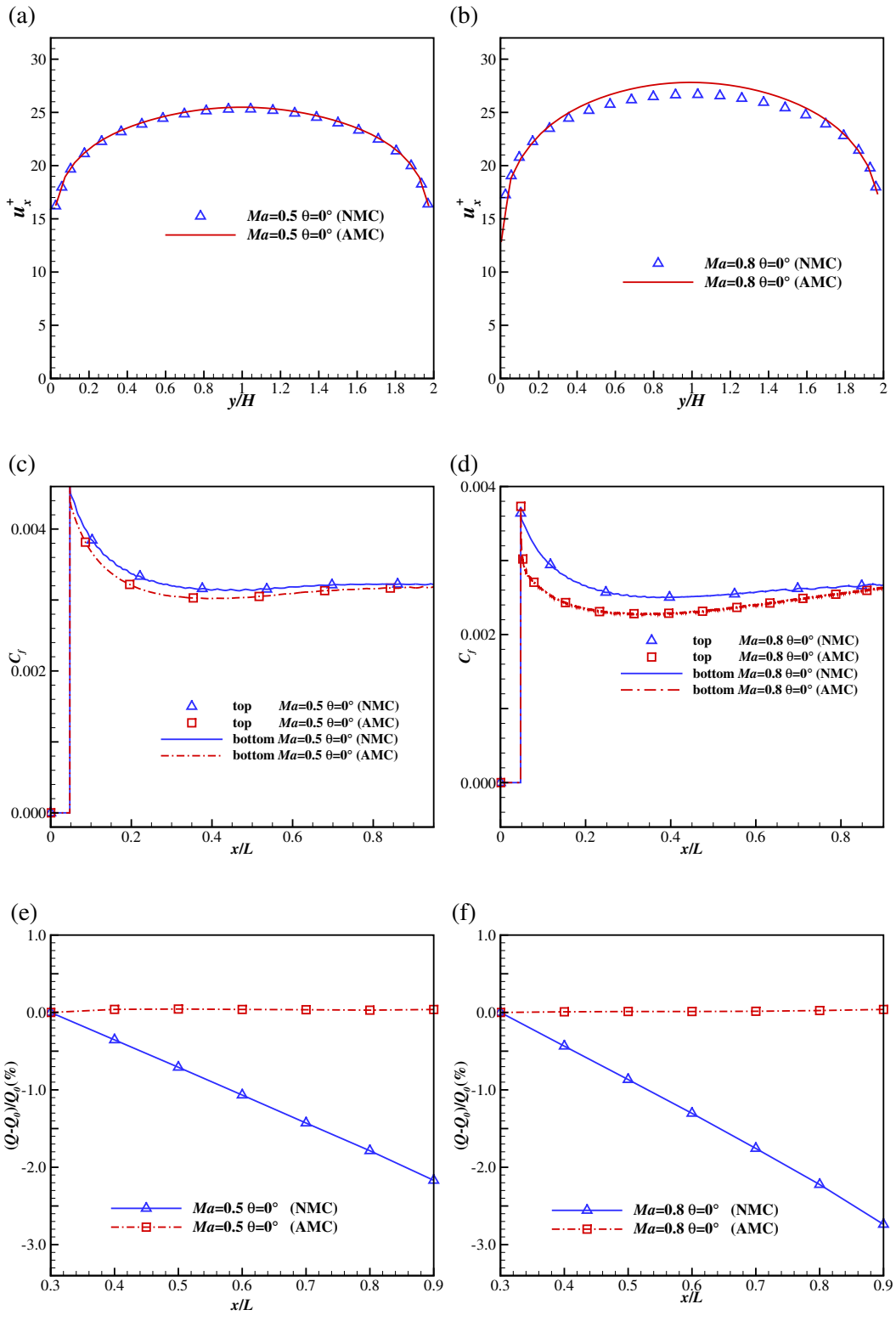

FIG. 3. The profiles of the sectional velocity, the skin friction and sectional mass flux variation at $Ma = 0.5$ and 0.8 for $\theta = 0°$.

can be attributed to mass leakage in the problem, and it can be effectively mitigated by applying mass correction (as demonstrated in Figure 4(a)).

The profiles of the skin friction along the channel at $\theta = 15^\circ$ and 30° are depicted in Figure 4(b), which reveals the significant discrepancies between the skin frictions at the top and bottom walls when mass correction is not applied. In addition, the difference increases with the increase of the inclination angle θ. In contrast, with mass correction, the differences between the skin frictions at top and bottom walls are notably diminished. To further illustrate the influence of the inclination angle on the skin frictions, the relative difference between skin frictions at top and bottom walls are computed as

$$\Delta C_f = \left\| C_{f,top} - C_{f,bottom} \right\| / C_{f,bottom}, \tag{27}$$

where $C_{f,top}$ and $C_{f,bottom}$ are respectively the skin frictions at the top and bottom walls. Figure 4(c) illustrates the relative differences in skin friction at $\theta = 15^\circ$ and 30° for $Ma = 0.2$. As depicted in the figure, the relative difference ΔC_f can surpass 10% and 30% for $\theta = 15^\circ$ and 30°, respectively, in the absence of mass correction. However, by applying mass correction, this difference can be reduced to below 5% in both inclination angles. Figure 4(d) illustrates the relative variants of the mass flux at different cross sections along the channel. It is observed that the mass flux experiences rising along the channel in both inclined cases different from the linear reduction in the aligned case ($\theta = 0^\circ$). In addition, the variant of the mass flux can respectively be over 1.6% and 0.6% at $\theta = 15^\circ$ and 30° with the correction on the mass leakage, compared with the prominently reduced variant (within 0.4%) for cases with mass correction. Similar tendency is also observed at $Ma = 0.5$ and 0.8 (Please find more details in Figure 5 and 6).

Overall, the mass leakage exists in the aligned cases at all Ma considered, but the mass leakage does not show significant influence on the profiles the cross-sectional velocity and the skin friction. In contrast, the mass leakage can be big issue when the inclination angle θ is not 0. The symmetric distribution of the cross-sectional velocity and skin friction is ruined, and the mass correction scheme can remarkably recover the symetric distribtions by mitigating the mass leakage.

B. The compressible turbulent flow in the NASA Glenn S-duct

In this section, the dynamics of compressible turbulent flow in a NASA Glenn S-duct are investigated. This case can serve as a benchmark validation case for complex three-dimensional

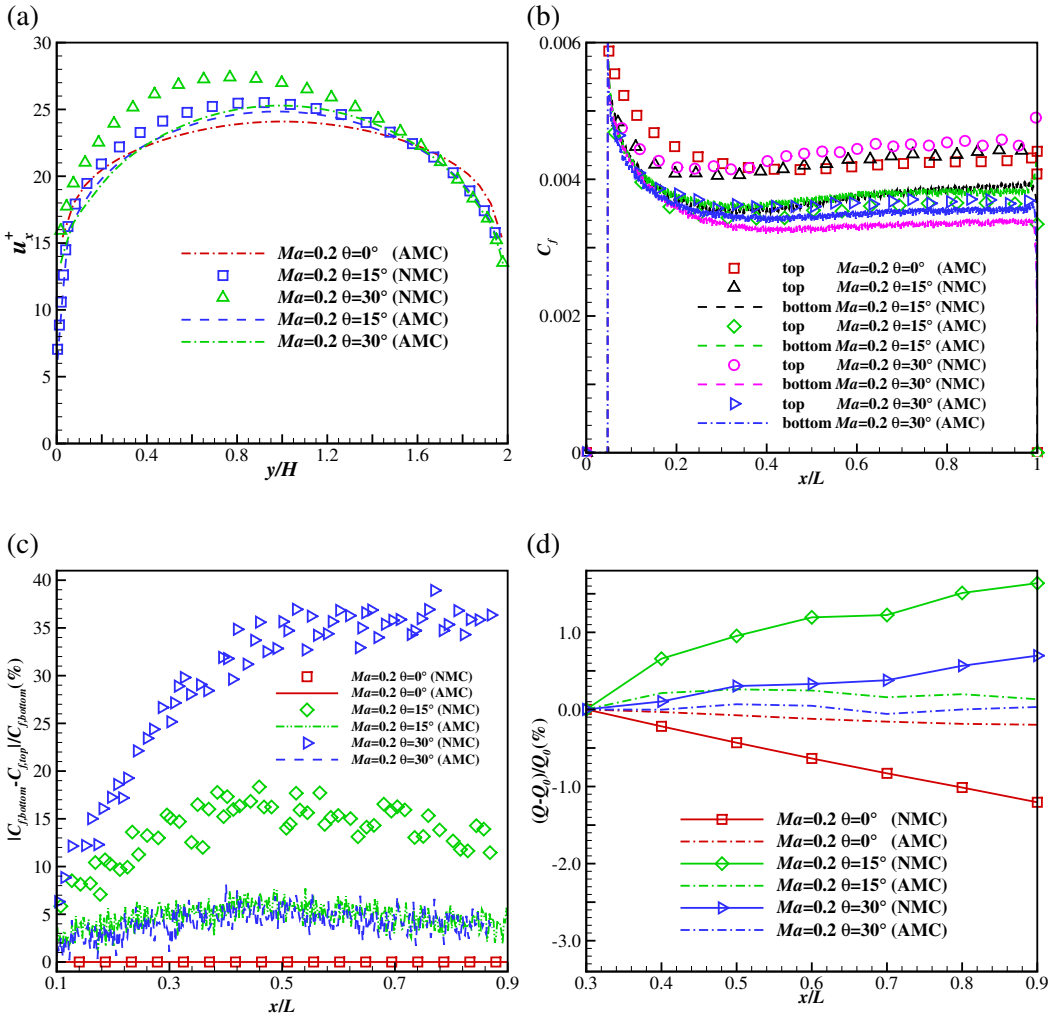

FIG. 4. The profiles of (a) the sectional velocity, (b) the skin friction and (c) the relative difference of the skin friction at $Ma = 0.2$ for $\theta = 15°$ and $30°$. (d) The sectional mass flux variation along the channel.

compressible flow phenomena such as boundary-layer separation and secondary flows[29,30]. In addition, as demonstrated in Section IV A, changing the grid's topology can result in significant mass leakage problems. Hence, the objective of this case also involves the examination of the mass leakage issue in three-dimensional compressible turbulent flow and evaluation on how the mesh's topology affects the symmetry of fluid properties. The centerline of the S-duct is created by combining two identical circular arcs, both of which have the same radius ($R = 1.02$ m) and are located in the same plane. Eqs. 28-30 are used to create the centerline of the duct (as show in Figure 7), with $\theta_m/2 = 30$ deg,

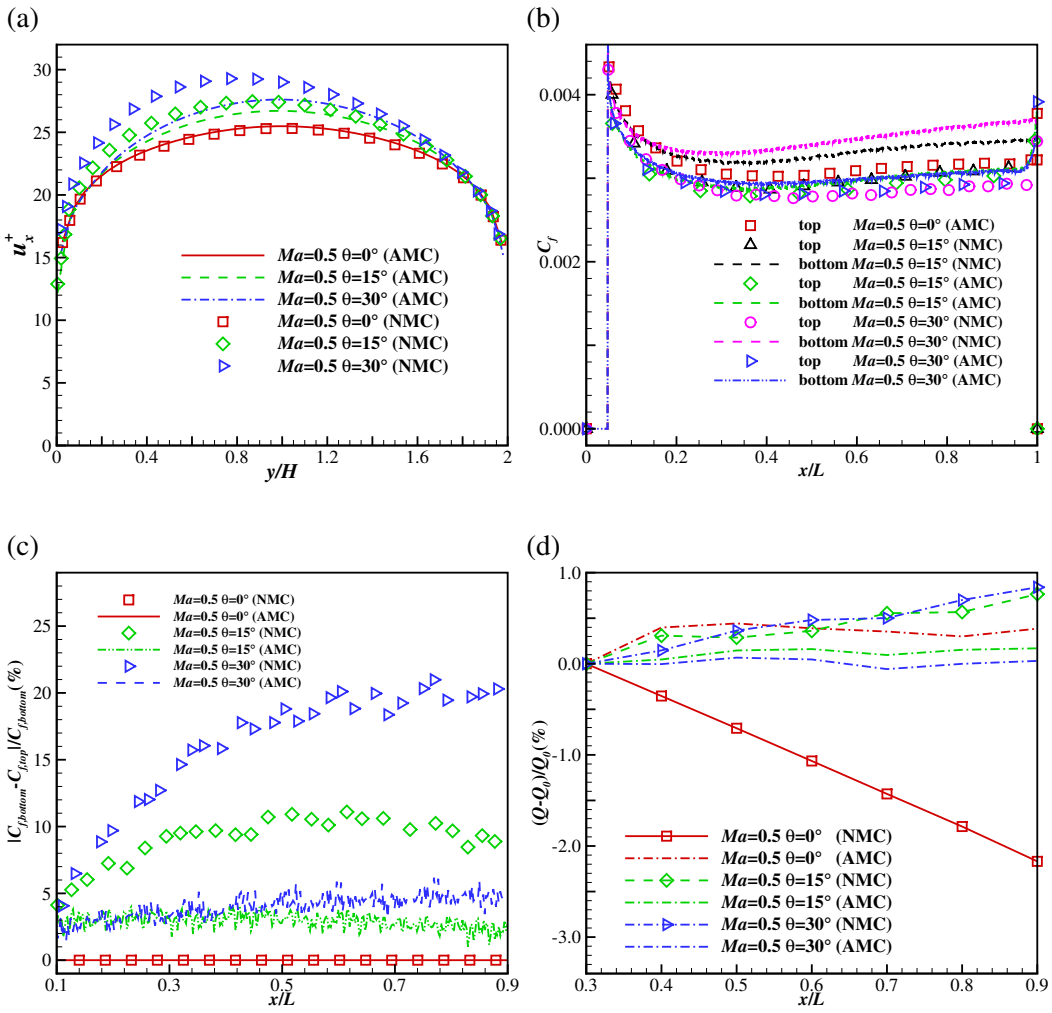

FIG. 5. The profiles of (a) the sectional velocity, (b) the skin friction and (c) the relative difference of the skin friction at $Ma = 0.5$ for $\theta = 15^\circ$ and 30°. (d) The sectional mass flux variation along the channel.

$$x_{cl} = \begin{cases} R\sin\theta, & \text{for } 0 \le \theta \le \frac{\theta_m}{2}, \\ 2R\sin\left(\frac{\theta_m}{2}\right) - R\sin\left(\theta_m - \theta\right), & \text{for } \frac{\theta_m}{2} \le \theta \le \theta_m, \end{cases} \tag{28}$$

$$y_{cl} = 0, \tag{29}$$

$$z_{cl} = \begin{cases} R\cos\theta - R, & \text{for } 0 \le \theta \le \frac{\theta_m}{2}, \\ 2R\cos\left(\frac{\theta_m}{2}\right) - R\left(1 + \cos\left(\theta_m - \theta\right)\right), & \text{for } \frac{\theta_m}{2} \le \theta \le \theta_m, \end{cases} \tag{30}$$

where x_{cl}, y_{cl}, and z_{cl} represent the coordinates of the centerline, with each variable corresponding to a specific dimension. The cross-sectional area of duct expands gradually along the centerline,

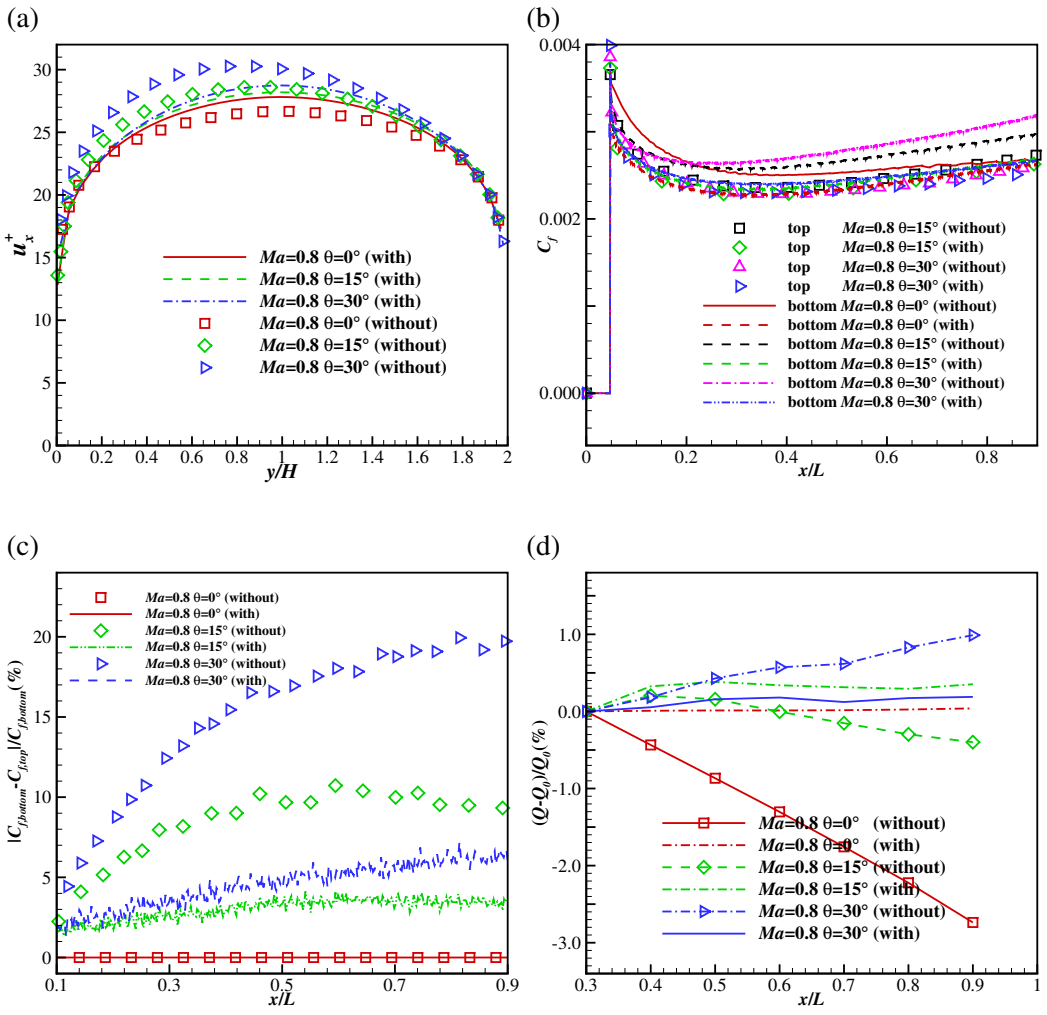

FIG. 6. The profiles of (a) the sectional velocity, (b) the skin friction and (c) the relative difference of the skin friction at $Ma = 0.8$ for $\theta = 15^\circ$ and 30°. (d) The sectional mass flux variation along the channel.

and the cross-sectional radius r is given by

$$\frac{r}{r_1} = 1 + 3\left(\frac{r_2}{r_1} - 1\right)\left(\frac{\theta}{\theta_m}\right)^2 - 2\left(\frac{r_2}{r_1} - 1\right)\left(\frac{\theta}{\theta_m}\right)^3, \tag{31}$$

where $r_1 = 0.1021$ m and $r_2 = 0.1257$ m are respectively radii of the inlet and outlet. Here, pipes with constant diameter of length 0.762 m are added to the front and aft of the convoluted duct to be consistent with the experiment configuration[29,31], and the surface of the S-duct generated and utilized in the simulations is illustrated in Figure 8. The uniform mesh is generated over the whole computational domain, and two different grid spacings (fine: $\Delta x = \Delta y = \Delta z = 0.002$ m and coarse: $\Delta x = \Delta y = \Delta z = 0.004$ m) are used, corresponding to 1.67 and 13.65 million grid nodes,

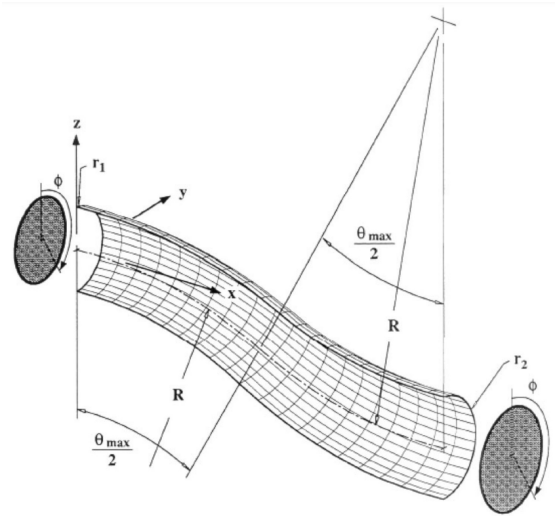

FIG. 7. The geometry of the NASA Glenn S-duct[29].

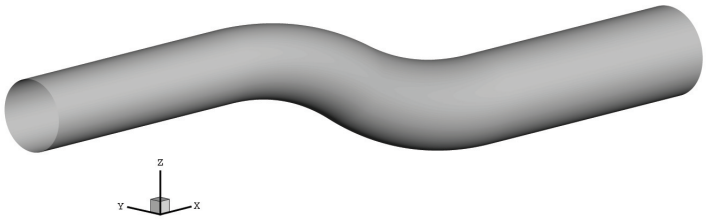

FIG. 8. The surface of the NASA Glenn S-duct.

respectively. In the simulations, the grid used is slightly adjusted to introduce a minor asymmetry in the mesh distribution.

The constant total mass flux is set at the inlet, and at the outlet, a constant pressure is applied. The surface of the S-duct is assumed to be non-slip adiabatic wall. The mass flow rate at the inlet is tuned to match the prescribed centerline Mach number $Ma = 0.6$ at the reference inlet, where the non-dimensional arc length along the centerline of the S-duct is $s/D_1 = -0.5$ (with $D_1 = 2r_1$ being the diameter of the inlet). Here, we examine the wall static pressure coefficient Cp along three streamwise lines on the surface of the S-duct, and it is calculated as[30,32]

$$C_p = \frac{p - p_{cl}}{p_{0,cl} - p_{cl}} \tag{32}$$

where p is the local static pressure, and $p_{o,cl}$ and p_{cl} are respectively the total and static pressure at the center of reference inlet cross section $s/D_1 = -0.5$.

First, the present results are validated against previous experimental[29] and numerical[30,32] results to confirm the accuracy of the present method. Figure 9 displays the profiles wall static pressure C_p along three streamwise lines ($\Phi = 10^\circ, 90^\circ$ and 170°) on the surface of the S-duct. It is observed that the present results generally show good agreement with the previous experimental and numerical results, which proves the accuracy of the present method in three-dimensional compressible flow in complex geometries.

Next, the issue of mass leakage in this problem and the effects of mesh topology on the results are examined. Figure 10(a) compares the profiles of static pressure (C_p) with and without mass correction for cases with a coarse mesh ($\Delta x = \Delta y = \Delta z = 0.004$ m). It can be observed that there is no significant difference in the results when the mass correction scheme is utilized. The sectional mass flux variation along the S-duct is illustrated in Figure 10(b), revealing minimal mass leakage in this problem. Additionally, Figure 11 displays the profiles of static pressure (C_p) on different halves of the S-duct. It is evident that there is no notable difference in wall static pressure between the two halves, indicating that the topology of the mesh does not significantly influence the results in this problem.

V. CONCLUSIONS

We have conducted a comprehensive numerical investigation of high subsonic compressible turbulent flows using the pressure-based lattice Boltzmann method in conjunction with the Spalart-Allmaras turbulent model. Our study focuses on evaluating the mass leakage issue in compressible turbulent flows and examining the effectiveness of the previously proposed averaged mass correction, initially intended for incompressible flows, by Xu *et al.*[19]. To this end, we have examined inclined straight channels and a NASA Glenn S-duct.

Our findings indicate that mass leakage can be a significant concern in compressible turbulent channel flows across all Mach numbers considered in this study ($Ma = 0.2, 0.5$, and 0.8), even in aligned channel cases where the mass leakage is negligible in incompressible turbulent flows. In aligned channel cases, where the mass leakage correction is absent, cross-sectional velocity and

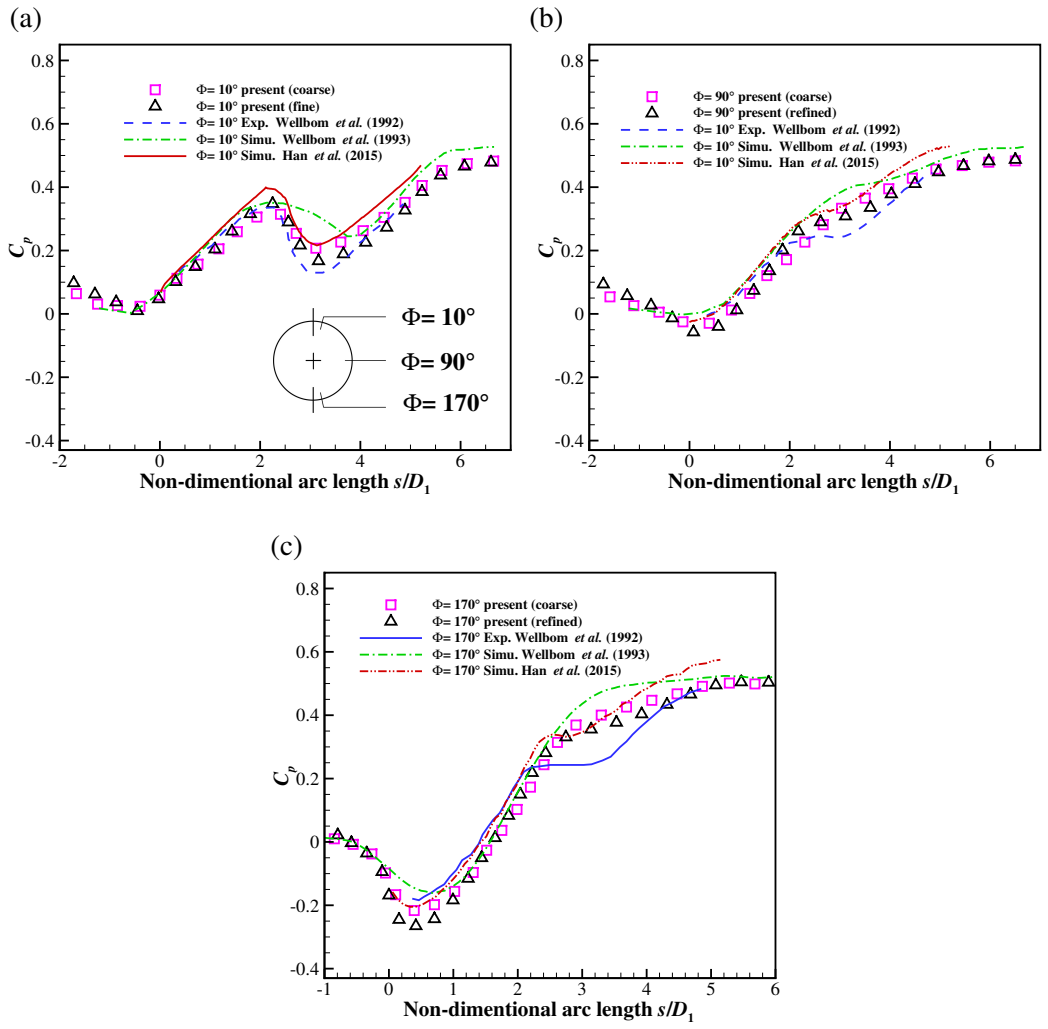

FIG. 9. The profiles of the wall static pressure C_p along three streamwise lines ($\Phi = 10°, 90°$ and $170°$) on the surface of the S-duct. Inset: the positions of surface nodes at three streamwise lines on a cross section of the S-duct.

skin frictions at the top and bottom walls exhibit symmetric distributions. However, the mass flux experiences a linear decrease along the channel. In inclined cases, the presence of mass leakage disrupts the symmetric distributions of cross-sectional velocity and skin frictions. By employing the mass correction, significant improvements are observed in the symmetry of skin friction and sectional velocity profiles.

Furthermore, we have investigated compressible turbulent flow in a NASA Glenn S-duct to evaluate the capability of our compressible solver in studying complex three-dimensional flows. The obtained results demonstrate good agreement with previous experimental and numerical data

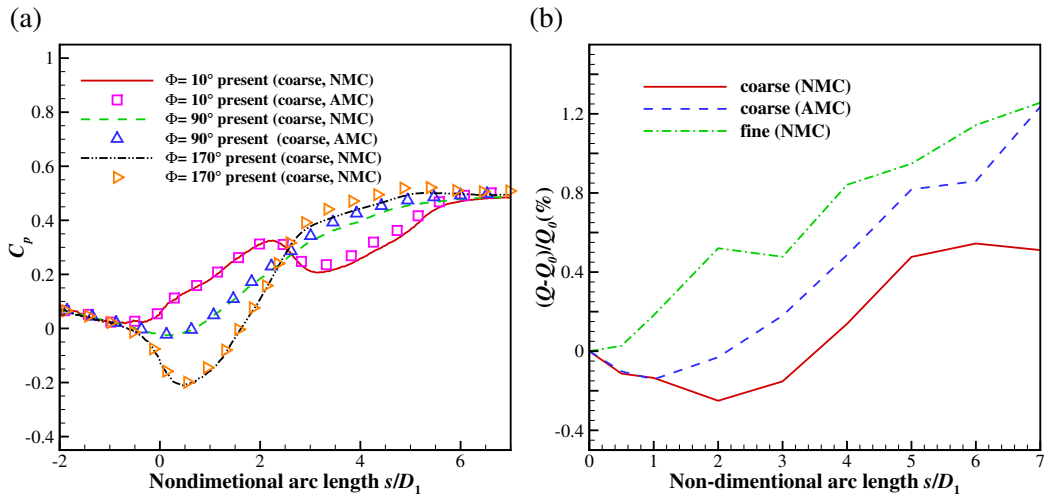

FIG. 10. (a): The comparison of profiles of the wall static pressure between NMC and AMC. (b):The sectional mass flux variation along the S-duct.

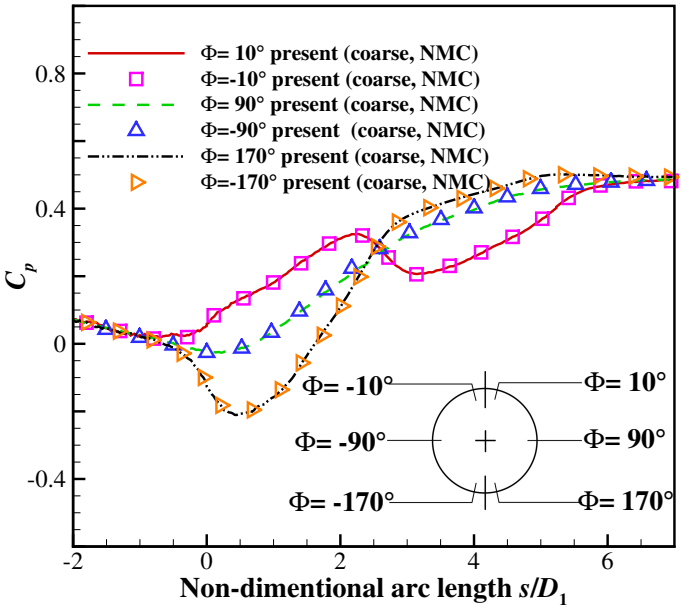

FIG. 11. The comparison of the wall static pressure Cp on two halves of the S-duct.

on the static pressure coefficient along three streamwise lines on the S-duct surface. This substantiates the effectiveness of our approach in capturing complex three-dimensional phenomena in compressible flows.

Overall, our study provides valuable insights into the behavior of compressible turbulent flows and highlights the significance of addressing the mass leakage issue. The proposed averaged mass

correction offers a promising solution for improving the accuracy and reliability of simulations in various practical scenarios.

ACKNOWLEDGMENTS

We wish to acknowledge the support of the author community in using REVTEX, offering suggestions and encouragement, testing new versions, ...

Appendix A: Appendixes

To describe the turbulent flow, the Spalart-Allmaras turbulence model is employed in this work. The Spalart-Allmaras model possesses considerable appeal because of its simplicity, reliability, and computational efficiency. Unlike the two-equation models that require calculations for turbulence time and length scales, the SA model directly computes the eddy viscosity. Additionally, it surpasses algebraic models in versatility by considering transport and historical effects.

In the Spalart-Allmaras model, a working viscosity $\tilde{\nu}$ is defined to preserve the linear relationship $\tilde{\nu} = \kappa u_\tau d$ (u_τ and d are respectively the friction velocity and the distance to the wall) all the way down to the wall, and the eddy viscosity is computed as

$$\nu_t = \tilde{\nu} f_{v1}, \tag{A1}$$

where f_{v1} is the damping function, defined as

$$f_{v1} = \frac{\chi^3}{\chi^3 + c_{v1}^3}, \tag{A2}$$

with $\chi = \tilde{\nu}/\nu$ (ν is the fluid kinematic viscosity) and $c_{v1} = 7.1$ being a constant in SA model.

To prevent the negative values of the source term, the SA model with a f_{v3} is utilized in this work[6,7], and the transportation equation for $\tilde{\nu}$ is given as

$$\frac{D\tilde{\nu}}{Dt} \equiv \frac{\partial \tilde{\nu}}{\partial t} + u_j \frac{\partial \tilde{\nu}}{\partial x_j} = c_{b1}\tilde{S}\tilde{\nu} + \frac{1}{\sigma}\left[\frac{\partial}{\partial x_j}\left((\nu + \tilde{\nu})\frac{\partial \tilde{\nu}}{\partial x_j}\right) + c_{b2}\left(\frac{\partial \tilde{\nu}}{\partial x_j}\right)^2\right] - c_{w1} f_w \left(\frac{\tilde{\nu}}{d}\right)^2 \tag{A3}$$

with the three terms on the right side of the equation being production, diffusion and destruction terms, respectively. Their components are computed as follows,

$$\tilde{S} = f_{v3}\Omega + \frac{\tilde{\nu}}{\kappa^2 d^2} f_{v2}, \quad \Omega = \sqrt{\frac{1}{2}\left(\frac{\partial u_i}{\partial x_j} - \frac{\partial u_j}{\partial x_i}\right)^2},$$
$$f_{v2} = \left(1 + \frac{\chi}{c_{v2}}\right)^{-3}, \quad f_w = g\left[\frac{1+c_{w3}^6}{g^6 + c_{w3}^6}\right]^{1/6}$$
$$g = r + c_{w2}\left(r^6 - r\right), \quad r = \min\left[\frac{\tilde{\nu}}{\tilde{S}\kappa^2 d^2}, 10\right] \tag{A4}$$
$$f_{v3} = \frac{(1+\chi f_{v1})(1-f_{v2})}{\chi}$$

with the constants being gives as

$$c_{b1} = 0.1355, \quad \sigma = \frac{2}{3}, \quad c_{b2} = 0.622, \quad \kappa = 0.41$$
$$c_{w1} = \frac{c_{b1}}{\kappa^2} + \frac{1+c_{b2}}{\sigma}, \quad c_{w2} = 0.3, \quad c_{w3} = 2, \quad c_{v2} = 5. \tag{A5}$$

REFERENCES

[1]A. Eshghinejadfard, L. Daróczy, G. Janiga, and D. Thévenin, "Calculation of the permeability in porous media using the lattice boltzmann method," International Journal of Heat and Fluid Flow **62**, 93–103 (2016).

[2]M. A. Spaid and F. R. Phelan Jr, "Lattice boltzmann methods for modeling microscale flow in fibrous porous media," Physics of fluids **9**, 2468–2474 (1997).

[3]Z. Guo and T. Zhao, "Lattice boltzmann model for incompressible flows through porous media," Physical review E **66**, 036304 (2002).

[4]Q. Huang, F.-B. Tian, J. Young, and J. C. Lai, "Transition to chaos in a two-sided collapsible channel flow," Journal of Fluid Mechanics **926**, A15 (2021).

[5]L. Xu, F.-B. Tian, J. Young, and J. C. Lai, "A novel geometry-adaptive cartesian grid based immersed boundary–lattice boltzmann method for fluid–structure interactions at moderate and high reynolds numbers," Journal of Computational Physics **375**, 22–56 (2018).

[6]S. Wilhelm, J. Jacob, and P. Sagaut, "An explicit power-law-based wall model for lattice boltzmann method–reynolds-averaged numerical simulations of the flow around airfoils," Physics of Fluids **30**, 065111 (2018).

[7]S.-G. Cai, J. Degrigny, J.-F. Boussuge, and P. Sagaut, "Coupling of turbulence wall models and immersed boundaries on cartesian grids," Journal of Computational Physics **429**, 109995 (2021).

[8]J. Ma, Z. Wang, J. Young, J. C. Lai, Y. Sui, and F.-B. Tian, "An immersed boundary-lattice boltzmann method for fluid-structure interaction problems involving viscoelastic fluids and complex geometries," Journal of Computational Physics **415**, 109487 (2020).

[9]T. Krüger, H. Kusumaatmaja, A. Kuzmin, O. Shardt, G. Silva, and E. M. Viggen, "The lattice boltzmann method," Springer International Publishing **10**, 4–15 (2017).

[10]C. K. Aidun and J. R. Clausen, "Lattice-boltzmann method for complex flows," Annual Review of Fluid Mechanics **42**, 439–472 (2010).

[11]Z. Wang, Y. Wei, and Y. Qian, "A bounce back-immersed boundary-lattice boltzmann model for curved boundary," Applied Mathematical Modelling **81**, 428–440 (2020).

[12]R. Mei, L.-S. Luo, and W. Shyy, "An accurate curved boundary treatment in the lattice boltzmann method," Journal of computational physics **155**, 307–330 (1999).

[13]M. Bouzidi, M. Firdaouss, and P. Lallemand, "Momentum transfer of a boltzmann-lattice fluid with boundaries," Physics of fluids **13**, 3452–3459 (2001).

[14]G. Zhao-Li, Z. Chu-Guang, and S. Bao-Chang, "Non-equilibrium extrapolation method for velocity and pressure boundary conditions in the lattice boltzmann method," Chinese physics **11**, 366 (2002).

[15]I. Ginzbourg and D. d'Humières, "Local second-order boundary methods for lattice boltzmann models," Journal of statistical physics **84**, 927–971 (1996).

[16]J. Bao, P. Yuan, and L. Schaefer, "A mass conserving boundary condition for the lattice boltzmann equation method," Journal of Computational Physics **227**, 8472–8487 (2008).

[17]P.-H. Kao and R.-J. Yang, "An investigation into curved and moving boundary treatments in the lattice boltzmann method," Journal of Computational Physics **227**, 5671–5690 (2008).

[18]E. Le Coupanec and J. C. Verschaeve, "A mass conserving boundary condition for the lattice boltzmann method for tangentially moving walls," Mathematics and Computers in Simulation **81**, 2632–2645 (2011).

[19]L. Xu, E. Serre, and P. Sagaut, "A theoretical analysis of mass leakage at boundaries within the lattice boltzmann method," Physics of Fluids **34**, 065113 (2022).

[20]G. Farag, S. Zhao, T. Coratger, P. Boivin, G. Chiavassa, and P. Sagaut, "A pressure-based regularized lattice-boltzmann method for the simulation of compressible flows," Physics of Fluids **32**, 066106 (2020).

[21]T. Coratger, G. Farag, S. Zhao, P. Boivin, and P. Sagaut, "Large-eddy lattice-boltzmann modeling of transonic flows," Physics of Fluids **33**, 115112 (2021).

[22]H. Yoo, M. Bahlali, J. Favier, and P. Sagaut, "A hybrid recursive regularized lattice boltzmann model with overset grids for rotating geometries," Physics of Fluids **33**, 057113 (2021).

[23]G. Wang, L. Xu, E. Serre, and P. Sagaut, "Large temperature difference heat dominated flow simulations using a pressure-based lattice boltzmann method with mass correction," Physics of Fluids **33**, 116107 (2021).

[24]Y. Feng, P. Boivin, J. Jacob, and P. Sagaut, "Hybrid recursive regularized thermal lattice boltzmann model for high subsonic compressible flows," Journal of Computational Physics **394**, 82–99 (2019).

[25]S. Guo, Y. Feng, J. Jacob, F. Renard, and P. Sagaut, "An efficient lattice boltzmann method for compressible aerodynamics on d3q19 lattice," Journal of Computational Physics **418**, 109570 (2020).

[26]J. Jacob, O. Malaspinas, and P. Sagaut, "A new hybrid recursive regularised bhatnagar–gross–krook collision model for lattice boltzmann method-based large eddy simulation," Journal of Turbulence **19**, 1051–1076 (2018).

[27]N. Afzal and K. Gersten, "Wake layer in a turbulent boundary layer with pressure gradient: a new approach," Fluid Mechanics and Its Applications **37**, 95–118 (1996).

[28]S. Hoyas and J. Jiménez, "Scaling of the velocity fluctuations in turbulent channels up to re τ= 2003," Physics of fluids **18**, 011702 (2006).

[29]S. WELLBORN, B. REICHERT, and T. OKIISHI, "An experimental investigation of the flow in a diffusing s-duct," in *28th Joint Propulsion Conference and Exhibit* (1992) p. 3622.

[30]S. R. Wellborn, B. A. Reichert, and T. H. Okiishi, "Study of the compressible flow in a diffusing s-duct," Journal of Propulsion and Power **10**, 668–675 (1994).

[31]M. M. Wojewodka, C. White, S. Shahpar, and K. Kontis, "Numerical study of complex flow physics and coherent structures of the flow through a convoluted duct," Aerospace Science and Technology **121**, 107191 (2022).

[32]X. Han, T. J. Wray, C. Fiola, and R. K. Agarwal, "Computation of flow in s ducts with wray–agarwal one-equation turbulence model," Journal of Propulsion and Power **31**, 1338–1349 (2015).